ISBN: 978-3-95450-250-9 ISSN: 2673-5520 doi:10.18429/JACoW-MEDSI2023-WEOBM05

THERMAL CALCULATION AND TESTING OF SLS 2.0 CROTCH ABSORBERS

Xinyu Wang†, Colette Rosenberg, Romain Ganter, André Weber, Markus Maehr, Samuel Bugmann
Paul Scherrer Institut, Villigen, Switzerland

Abstract

After 22 years of operation, the Swiss Light Source (SLS) was recently shut down on September 30, 2023, and the construction of SLS 2.0 has commenced. The storage ring of SLS2.0 based on a multibend achromat lattice will have the maximum electron energy of 2.7 GeV. SLS 2.0 crotch absorbers are designed to have two water-cooled, toothed jaws made of Glidcop to dissipate a maximum heat power of 6 kW. Finite element analysis has been conducted to validate the thermal and mechanical strength of the absorber's mechanical design. A conjugate heat transfer (CHT) simulation was performed to verify the water cooling concept. Furthermore, a prototype absorber underwent testing in an e-beam welding chamber. This paper describes numerical simulation and thermal testing of SLS 2.0 absorber.

INTRODUCTION

The storage ring of SLS 2.0 will feature a 40-fold increase in hard X-Ray brilliance, achieved through a low-emittance magnet lattice and a beam pipe with smaller aperture [1, 2]. The majority of over 100 pieces of absorbers is designated to dissipate synchrotron radiation power from normal bend dipoles [3]. The normal incidence power density is at a maximum of 600 W/mm^2 for a total power up to 3.5 kW. This absorber was initially designed using the age-hardenable CuCrZr alloy with two individually water-cooled upper and lower parts with saw-tooth surfaces. The idea was to produce the absorbers by wire erosion with a directly machined Conflat type knife edge in the absorber body. As no welding or brazing procedure would be necessary, this was expected to reduce material and fabrication costs [4-6]. From the 5 T superconducting magnets, a total power of about 7 kW is generated with the normal incidence power reaching as high as 1100W/mm^2. A different design and material is required, and Glidcop® AL-15 alloy was chosen due to its higher thermal conductivity and better resistance to thermal stress. The jaw has an inclination of 1° with a number of flat teeth and intermediate grooves. The teeth of upper and lower jaws interleave without contacting each other. In this way, the power was distributed to the upper and lower jaws, so that the power density is reduced to less than 30 W/mm^2. The two jaws are water-cooled and brazed into a stainless-steel flange.

WATER COOLING MODELLING

The cooling concept of SLS1 absorber has been adapted: the inlet water is guided by a stainless steel tube to the end of the pin hole and flows back through the helical channel on outer surface of the tube. Each jaw has three 10 mm pin-holes, and the tube has a diameter of 6 mm (inner) and 8 mm (outer). The average water velocity is limited to 1.5 m/s due to corrosion concerns, which corresponds to a flow rate of 15.3 l/min for an absorber with 6 channels.

In thermal calculations, water cooling can be simulated as forced convection using a heat transfer coefficient with a constant water temperature. Alternatively, water flow can be modeled using 1D thermal fluid elements, taking into account temperature changes in the water. For most common pipe geometries and flow conditions, the heat transfer coefficient can be estimated from correlations, such as Dittus-Boelter, Sieder-Tate, etc. Ultimately, the Computational Fluid Dynamics (CFD) analysis can be employed to investigate heat transfer between the solid and fluid.

A conjugate heat transfer simulation of a full absorber body including six stainless steel water pipes in parallel and with fluid water, would be very complex and time-consuming. Therefore a sub-model contains one water pipe with the lower-left part of the absorber, which removes more than ¼ of total heat power, has been analysed [7]. The Fluent model contains 3.7 million zones and 9.5 million nodes for the fluid, and 197'000 zones and 847'000 nodes for the solid. The turbulence model used was SST k-omega.

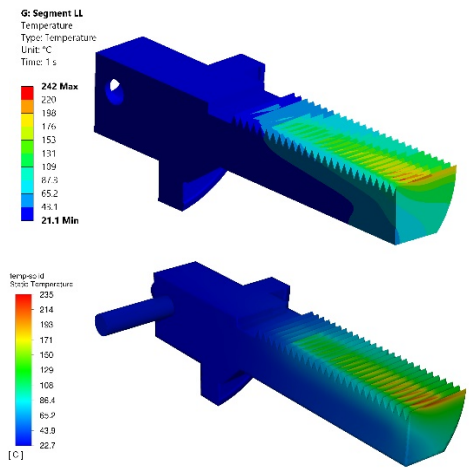

Figure 1: Temperature distribution in °C, from a): mechanical thermal model (top) and b): CFD model (bottom).

The adiabatic boundary condition was applied on the horizontal cutting face, as heat transfer between the upper and lower parts of the absorber is negligible. On the vertical section face, a convective boundary condition was applied to simulate the heat transfer to the colder, cut portion of the absorber jaw. Further simplification includes uniform distribution of heat flux on the surfaces. The thermal

† Xinyu.wang@psi.ch

ISBN: 978-3-95450-250-9 ISSN: 2673-5520 doi:10.18429/JACoW-MEDSI2023-WEOBM05

calculation with the sub-model closely represents the temperature distribution in the global model.

Figure 1a) shows the temperature distribution on the absorber body, calculated from thermal analysis with a heat transfer coefficient of 15 kW/(m^{2}K) and a constant water temperature of 25 °C. Fig. 1b) is calculated from CFD analysis with an inlet water temperature of 25 °C and a velocity of 1.5 m/s. The outlet water temperature is calculated to be 30.3 °C. The maximum temperature from mechanical thermal analysis is slightly higher than that from CFD calculation by 3%. This verifies the accuracy of cooling parameter in the thermal model.

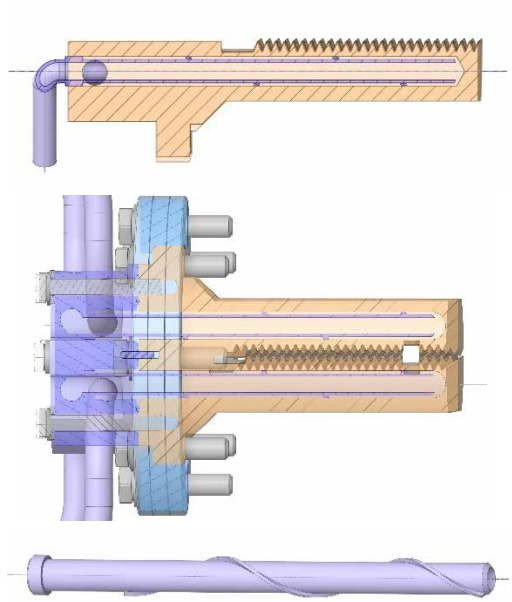

Figure 2: Cooling water channel, a) CFD model water returns at conical end (top), b) Cross section of prototype absorber, water channel with spherical end (middle), c) water pipe with integrated guide (bottom).

The pressure drop in one channel from CFD calculation is 11.5 kPa, primarily due to flow direction reversal at the end of the channel. The maximum velocity reached 3.5 m/s after flow direction reversal. The swirl flow was recognized immediately after flow returned and crossed helical coil on the outside of water tube, which guides the water flow and fix the cooling pipe to the surface of absorber's water channel. The conical shape at the end of water channel is then modified to spherical shape, as shown in Fig. 2b). In addition, the helical coil is replaced by machining the channel guide into stainless steel tube (Fig. 2c)). These design modifications will enable a smooth and stable attachment of water tube and reduce vibrations caused by water flow.

PROTOTYPE ABSORBER

Thermal Test

The prototype absorber made of CuCrZr, was tested in an e-beam welding chamber at PSI mechanical workshop. The absorber was turned vertically, with e-beam coming from the top (Fig. 3). The upper jaw was facing the front and could be observed via a view window of the vacuum chamber. The absorber was fixed by clamping the two inlet stainless steel water pipes. A precisely angle alignment of welding beam to the absorber was difficult. Power was applied on the top surface of the front jaw in the picture (Fig. 3). Rather than distributing the power across the teeth of both jaws, it was concentrated on the side wall of a single jaw. In addition, the water velocity was low due to restrictions from the chiller. While we did not replicate the exact conditions with synchrotron radiation, this test provided valuable information about the cooling effect and was used for comparison with simulations.

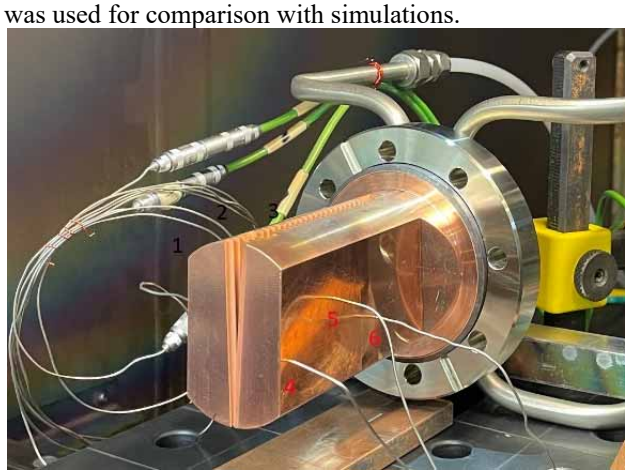

Figure 3: Thermal test in e-beam welding chamber on a prototype absorber.

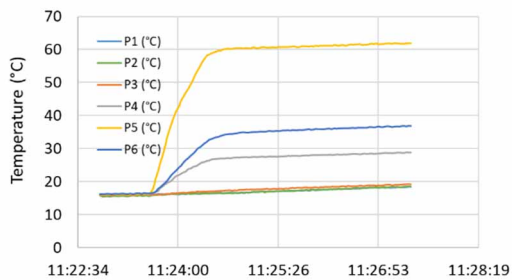

Figure 4: Temperature at absorber body with heat power 2790 W and flow rate 6.2 l/min.

From a calibration measurement, 75% of incident e-beam power was transmitted to heat power. The inlet and outlet water temperatures and temperatures on the absorber body at six locations were measured.

The measurement was started by shifting the e-beam position at a constant flow rate of 5.2 l/min. At each position, the heating process took several minutes until the temperature stabilized and steady-state heat transfer was achieved (Fig. 4). After reaching the final position, the total flow rate was switched to 6.2 l/min. After reached to the maximum flow rate of 6.7 l/min at the test site, it was reduced to 4.1 l/min. The inlet water pressure was 3.6 bar. The maximum heat power during the test reached 3 kW on the half of absorber, corresponding to 6 kW on a full absorber. No damage was observed in the visual inspection after the test.

ISBN: 978-3-95450-250-9 ISSN: 2673-5520 doi:10.18429/JACoW-MEDSI2023-WEOBM05

Thermal Simulation of the Test

The observed e-beam spot diameter was 10 mm. As the exact power density distribution of electron beam is unknown, calculations with different beam sizes have been performed to investigate their influence on the temperature measurement. It was found that by reducing the beam size from 10 mm to 6 mm, which corresponds to a reduction of projection area from 82 mm^2 to 31 mm^2, the maximum temperature on the absorber body increased significantly from 710 °C to 1080 °C. The hotspot temperature at the beam footprint was resulted from the test conditions in the welding chamber, where concentrated power was applied, and it did not match the real conditions in the storage ring. Thermal sensors were inserted through holes to surfaces very close to water channel. From thermal calculations, temperatures at these positons were independent of beam spot size (ΔT<0.1 °C). Therefore, the uncertainty in the power density of the e-beam has no impact on the temperature measurement. In the thermal calculation, the heat power of 2790 W was applied with a 6 mm beam, corresponding to 90.6 W/mm^2 on the projection area.

Figure 5 shows the thermal model. 1D fluid elements were used to simulate the water flow, which was simplified as straight flow. With a total flow rate at 6.7 l/min for example, the cooling water from the heated jaw was heated up by 11 °C from the measurement, close to the estimated value of 12 °C. The water temperature increase, however, was not equal for each channel. While the water temperature in the lowest channel away from the beam spot increased only slightly, it was heated up by 27 °C in the channel closest to the beam spot, as suggested in the calculation. Increased water temperature is able to be considered with 1D fluid elements in the convective heat transfer modeling, enables the temperature calculation with improved accuracy. Where the outlet water temperature increase is high, for example, more than 10 °C, it is advantageous to consider the use of fluid elements.

With a heat transfer coefficient of 15.5 kW/(m^2K) for flow rate 6.7 l/min, good correlation between calculation and measurement temperatures was achieved. According to Dittus-Boelter correlation, the heat transfer coefficient h is related to fluid speed v by: $h \sim v^{0.8}$ for turbulence water flow. The heat transfer coefficients for other flow rates were calculated with this relationship, as displayed in Fig. 6.

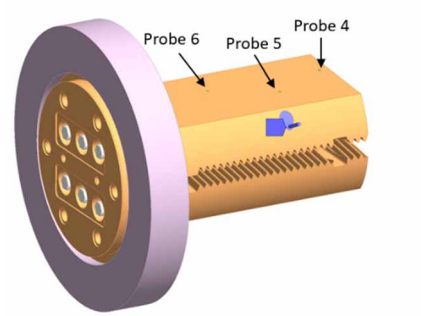

Figure 5: Thermal model, water flow is modelled as straight 1D fluid element.

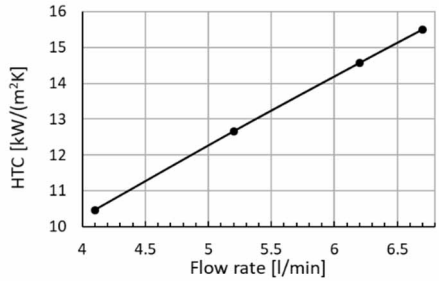

Figure 6: Teat transfer coefficient (HTC) versus flow rate.

Figure 7 displays the measured and calculated temperatures at thermal sensors 4, 5 and 6 on the heated jaw. Temperatures measured by sensors 1 to 3 was only slightly higher than the inlet water temperature. Probe 5 was the closest one to the beam spot, and the highest temperature was measured there. Probe 6 was closer to the beam spot than probe 4 and had a higher temperature.

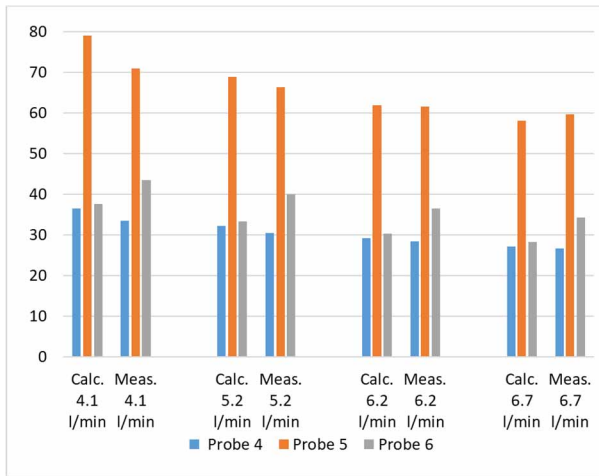

Figure 7: Temperature [°C] of thermal sensors 4, 5 and 6, from calculation and measurement and with different flow rates.

Because a very high power density was assumed in the simulation, the temperature on the water channel surface was calculated to be above 280 °C. This significantly exceeds the water saturation temperature of 140 °C at 3.6 bar [8], and phase transition to vapor is expected. Once phase transition is initiated, the mechanical thermal model is no longer valid for predicting local temperature. Thermal modelling in this calculation, however, is found to be useful for predicting temperature distribution on absorber body in correlation with flow rate in the range of this test. The water velocity in the thermal test reached up to 0.6 m/s, which was well below the designated water velocity for operation at 1.5 m/s. Nonetheless, a significant amount of heat transfer was achieved with flow boiling. The measurement shows that the prototype absorber is capable of withstanding a heat load of 3 kW on the half of absorber in a stable steady-state thermal condition.

ISBN: 978-3-95450-250-9 ISSN: 2673-5520 doi:10.18429/JACoW-MEDSI2023-WEOBM05

ABSORBER SIMULATIONS

Absorber Design

For a total power of 7 kW from the 5 T superconducting magnets Glidcop® AL-15 alloy, due to its high thermal conductivity and material strength, must be used. To sufficiently spread the SR power, the absorber has two jaws with interleaved flat teeth and intermediate grooves. As a consequence of the small opening angle of only 2 degrees, the vertical electron beam orbit offset is limited within +/-250 μm. The first absorber has a window opening and absorbs 5.9 kW of power. The rest of the initial 7 kW was sent to a second absorber a few meters downstream, which can be transversally aligned for fine adjustment of pointing direction.

In the manufacturing process, all components, including the jaws, flange, water distributor, and water pipes, are assembled and brazed together in a single operation. After the manufacturing process, quality assurance tests are conducted. Since the cost of the CuCrZr and Glidcop absorber versions were comparable, it was decided to choose Glidcop for all absorbers.

Thermal-Mechanical Models

Power density distributions on absorber surfaces has been calculated from SYNRAD simulation [3]. In thermal mechanical calculations with ANSYS Workbench, spatial heat power density distribution was defined as surface heat flux using APDL script. Due to the large number of faces, a MATLAB program was used to generate APDL script from SYNRAD output power data. It also converted the data into the desired format for ANSYS solver. This approach enabled fast and efficient data transfer from SYNRAD to ANSYS.

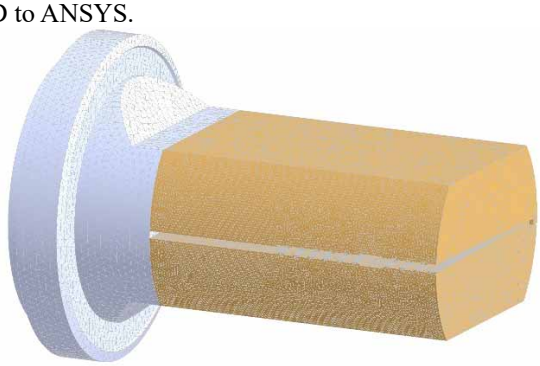

Figure 8: Finite element model of absorber.

To minimize the mapping error on surfaces with high power density, a mesh seed size of 0.2 mm was chosen, which was smaller than the SYNRAD mesh size.

For the remaining irradiated surfaces, the mesh seed size was 0.8 mm, while the general mesh size of the model was 2 mm. The finite element model consisted of a total of 3 million nodes and 2 million elements (Fig. 8).

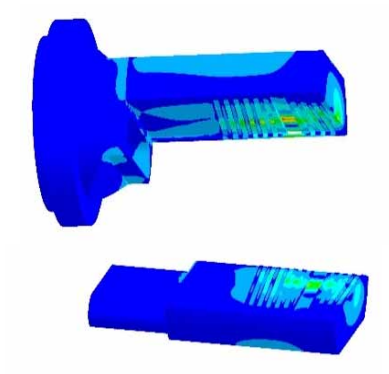

Figure 9: Thermal stress of absorber.

In the finite element analysis, stress, thermal deformation and temperature of absorber were calculated and verified against design criteria (Fig. 9). The maximal temperature on absorber surface was below 300°C and maximal thermal stress was about 200 N/mm^2. The maximum strain was 0.16% and below 0.2% for 10^5 heat loading cycles. The maximal cooling water temperature was limited to 160°C, below the water boiling temperature at 6 bar.

CONCLUSIONS

Comparison of the mechanical thermal calculation with a Fluent CFD simulation shows that the thermal model is capable of simulating the water-cooled absorber under specified heat load. When the heat load is high and water temperature increases significantly, 1D fluid elements may be used to account for heat transfer from the solid with increased water temperatures. For extreme heat loads involving phase transition, CFD simulation is necessary.

In a prototype thermal test, the temperatures of the absorber and cooling water were measured and compared against calculated values. The heat power in the test was much more concentrated, and the water flower was lower than in the real situation with synchrotron radiation. The absorber withstood the 3 kW power on a single jaw without visible damage. The test results validate the absorber's ability to dissipate the specified heat load and the cooling water's capacity to remove the heat. Furthermore, the final calculation verifies that the absorber temperature and stress meet the design requirements.

ACKNOWLEDGEMENTS

The authors kindly acknowledge Demian Lauper from CADFEM for his consultancy in CFD modelling.

REFERENCES

[1] H. Braun *et al.*, “SLS 2.0 storage ring. Technical design report”, Paul Scherrer Institut, Villigen, Switzerland (PSI Bericht, Rep. No.: 21-02).

[2] R. Ganter *et al.*, “SLS 2.0 Vacuum components design”, in *Proc. IPAC’23*, Venice, Italy, 2023, pp. 2726-2729. doi:10.18429/JACoW-IPAC-23-THPA147

[3] C. Rosenberg *et al.*, “SLS 2.0 Crotch absorbers design”, in *Proc. IPAC’23*, Venice, Italy, 2023, pp. 2730-2733. doi:10.18429/JACoW-IPAC-23-THPA148

ISBN: 978-3-95450-250-9 ISSN: 2673-5520 doi:10.18429/JACoW-MEDSI2023-WEOBM05

[4] F. Thomas *et al.*, "X-Ray Absorber Design and Calculations for the EBS Storage Ring", in *Proc. MEDSI'16*, Barcelona, Spain, Sep. 2016, pp. 257-261. doi:10.18429/JACoW-MEDSI2016-WEAA02

[5] M. Quispe, "Development of the Crotch Absorbers for ALBA Storage Ring" in *Proc. MEDSI'08*, Canada.

[6] F. A. DePaola, C. Amundsen, and S. K. Sharma, "Manufacturing of Photon Beam-Intercepting Components from Cu-CrZr", in *Proc. MEDSI'16*, Barcelona, Spain, Sep. 2016, pp. 233-235. doi:10.18429/JACoW-MEDSI2016-TUPE31

[7] D. Lauper, "CHT Simulation eines Kühlkanals", CADFEM Technical Report CON-20-PAU-001_TB1, 2000.

[8] W. Wagner *et al.,* "D2.1 Properties of water and steam", in *VDI Heat Atlas,* Springer, Berlin, Heidelberg, Apr. 2016. doi:10.1007/978-3-540-77877-6_11